Research Square

Preprints are preliminary reports that have not undergone peer review.
They should not be considered conclusive, used to inform clinical practice,
or referenced by the media as validated information.

Engineering edge-rich, highly dispersed, and stable MoS_2 sites for the catalytic splitting of H_2S for H_2 production

Pedro Castaño

pedro.castano@kaust.edu.sa

King Abdullah University of Science and Technology (KAUST) https://orcid.org/0000-0002-6454-9321

Hend Mohamed

King Abdullah University of Science and Technology (KAUST)

Vijay Velisoju

King Abdullah University of Science and Technology (KAUST) https://orcid.org/0000-0003-1182-8332

Mohammed Obaid

King Abdullah University of Science and Technology (KAUST)

Rafia Ahmed

King Abdullah University of Science and Technology (KAUST)

Yuma Hirayama

University of Osaka

Mohamed Hassine

King Abdullah University of Science and Technology (KAUST)

Gontzal Lezcano

King Abdullah University of Science and Technology (KAUST)

Ildar Mukhambetov

KAUST

Zainab Alaithan

Saudi Aramco

Muhammad Shafarifky

King Abdullah University of Science and Technology (KAUST)

Ali Almofleh

Saudi Aramco

Polina Tolstova

King Abdullah University of Science and Technology (KAUST) https://orcid.org/0000-0002-3646-6211

Omar El Tall

King Abdullah University of Science and Technology (KAUST)

Takato Mitsudome

Osaka University https://orcid.org/0000-0003-3071-8243

Huabin Zhang

King Abdullah University of Science and Technology https://orcid.org/0000-0003-1601-2471

Luigi Cavallo

King Abdullah University of Science and Technology https://orcid.org/0000-0002-1398-338X

Noreddine Ghaffour

King Abdullah University of Science and Technology (KAUST)

Hassan Aljama

Saudi Aramco

Article

Keywords: MoS2, H2S decomposition, electrospinning, hydrogen, nanofiber

Posted Date: March 4th, 2026

DOI: https://doi.org/10.21203/rs.3.rs-8597696/v1

License: This work is licensed under a Creative Commons Attribution 4.0 International License.
Read Full License

Additional Declarations: There is **NO** Competing Interest.

Abstract

Hydrogen sulfide (H_2S) decomposition offers a carbon-neutral route for hydrogen production, but it remains limited by sluggish kinetics and catalyst deactivation. Here, we report an electrospinning–sulfidation strategy to engineer a confined molybdenum disulfide (MoS_2) catalyst with stable edge-rich active sites. During electrospinning, confined Mo–S_4^{2-} complexes are dispersed within the nanofibers, which then nucleate into MoS_2 during calcination. The sulfidation stage induces exfoliation, forming highly dispersed MoS_2 domains that interact strongly with the carbon nanofibers. The prepared catalyst has a high surface area (~ 180 m^2 g^{-1}), abundant sulfur-vacancy edge sites, and strong support interactions, stabilized by coordinated Mo atoms. In-situ spectroscopy and ab-initio calculations reveal that these interfaces facilitate H_2S dissociation, leading to a 3-fold higher intrinsic rate and improved long-term stability (> 50 h at 973 K) compared to bulk analogues. This work establishes design principles for fabricating grafted, stable, and highly dispersed sulfide catalysts.

INTRODUCTION

Catalyst design for industrial hydrogen production requires precise control over the structure of the active sites, mechanistic insights derived under realistic conditions, and scalability without performance loss.[1,2] These requirements are particularly important for the catalytic splitting of hydrogen sulfide (H_2S),[3,4] which is a promising alternative to the energy-intensive Claus process.[4,5] Despite its simplicity, this endothermic reaction remains kinetically sluggish and prone to deactivation due to the high sulfur partial pressure and temperature required. Molybdenum disulfide (MoS_2) is the most widely studied catalyst for the splitting of H_2S due to its intrinsic tolerance to sulfur and its versatile chemistry.[6–9] However, the basal planes of layered MoS_2 prepared using the standard hydrothermal method are inaccessible,[5,10] and the edge sites responsible for S–H bond activation are difficult to engineer, prone to sintering, and can be deactivated through vacancy “healing” under standard reaction conditions.[4]

Overcoming these limitations requires the use of other supports and synthesis routes.[11–14] For example, carbon supports can enhance dispersion and stabilize sulfides,[15–18] while electrospinning can be used to more efficiently graft sulfide sites.[19] In particular, the electrospinning–reduction–sulfidation route can be employed to transform MoS_2 into a hierarchical dual-structure catalyst consisting of (i) extended monolayer MoS_2 nanosheets conformally anchored to carbon nanofibers (CNFs) and (ii) atomically deposited MoS_2 stabilized by the CNFs. Molecularly dispersing the Mo–S_4^{2-} precursor in polyacrylonitrile (PAN) during electrospinning leads to sulfide grafting and limits nanoparticle growth. Subsequent sulfidation induces exfoliation, preventing restacking and seeding atomic-limit MoS_2 on the CNFs.

In this work, we compare an electrospun catalyst (MoS_2|CNF-ES) with a hydrothermal bulk analogue (MoS_2–HT), a hybrid electrospinning–hydrothermal material (MoS_2–HT/CNF), and commercial bulk MoS_2 (MoS_2–Comm). Combined spectroscopic, microscopic, and kinetic analyses demonstrate that

electrospinning enabled more precise MoS_2 site engineering, enabling stable operation in highly concentrated H_2S environments. This work establishes a method for the accurate engineering of transition-metal sulfides with a high dispersion and defect density for high-temperature H_2S waste valorization and the production of C-free hydrogen.

RESULTS

Synthesis and structural evolution of MoS_2 catalysts: To elucidate how synthesis dynamics regulate active-site accessibility and catalytic stability, we prepared a series of MoS_2 catalysts, including the proposed electrospun catalyst (MoS_2|CNF-ES), a hydrothermal analogue (MoS_2–HT), a hybrid electrospinning–hydrothermal material (MoS_2–HT/CNF), and a commercial reference (MoS_2–Comm) (Methods and Fig. 1). In the electrospinning route, ammonium tetrathiomolybdate (ATTM) and PAN were dissolved in N,N-dimethylformamide (DMF) and subjected to electrohydrodynamic stretching under a high electric field, which immobilized the Mo–S_4^{2-} complexes along the fiber axis. This restricted precursor mobility and suppressed plane growth and stacking during the subsequent transformation (Fig. 1a). Under reductive carbonization at 723 K, ATTM decomposed within the CNF scaffold to form few-layered MoS_2 clusters (Fig. 1a). Subsequent sulfidation in $H_2S/H_2/N_2$ at 973 K induced exfoliation, yielding two types of MoS_2 sites: (i) monolayer MoS_2 slabs conformally anchored to the CNFs and (ii) atomically dispersed MoS_2 stabilized within the support (Fig. 1a). This synthesis route exploited growth control and support interaction to produce a monolayer, edge-enriched MoS_2 catalyst with unique features (see Supplementary Fig. S1a for more details).

The electrospinning parameters, including the polymer concentration, were systematically optimized to balance the CNF integrity, precursor dispersion, and final MoS_2 loading. PAN concentrations of 5–15 wt/vol% were evaluated, with 10 wt/vol% PAN yielding the most uniform fibers (Figs. S1–S3). In contrast, hydrothermal nucleation (MoS_2–HT; Fig. 1c) produced densely stacked 2H-MoS_2 lamellae (Fig. S4), while the physically mixed MoS_2–HT/CNF (Fig. 1b) exhibited intermediate behavior, with few-layered MoS_2 structures on the CNF surface. Together with MoS_2–Comm, these materials constituted a structural continuum ranging from a bulk multilayer material to atomically thin, edge-rich MoS_2 (Fig. 1 and Table S1).

Powder X-ray diffraction (XRD) analysis of MoS_2|CNF–ES revealed only in-plane (100) and (110) reflections of 2H-MoS_2 at $2\theta = 32.3°$ and 57.0°, respectively, whereas the characteristic (002) basal-plane reflection at 14.5° was almost completely suppressed (Fig. 1), confirming the absence of long-range stacking and the dominance of monolayer or highly exfoliated MoS_2.[20] This structural signature likely originated from the electrospinning environment, in which electrohydrodynamic stretching and rapid solvent evaporation immobilized Mo–S_4^{2-} complexes within the polymer jet. The resulting limited stacking dispersed the precursor at the nanoscale level, avoiding large flakes. During sequential reduction and sulfidation, ATTM decomposed, combined with gas-evolution-driven expansion and sulfur-

mediated layer delamination, further suppressing plane growth and stacking, yielding exfoliated MoS_2 sheets firmly anchored to the CNFs. In contrast, both MoS_2–HT and MoS_2–Comm. exhibited intense (002) reflections, while MoS_2–HT/CNF contained a (002) peak of moderate intensity, which was consistent with heterogeneous nucleation, controlled growth, and limited stacking (Fig. 1d and Figs S1–S4).

These findings were in accordance with the Raman spectroscopy analysis (Fig. 1e and Figs. S3 and S4). In the commercial and bulk MoS_2 samples, pronounced E_2g^1 (~ 380 cm^{-1}) and A_1g (~ 405 cm^{-1}) modes were observed. However, for the CNF-supported catalyst (MoS_2|CNF–ES), these MoS_2 phonons were not detectable because the strong D- and G-bands of the PAN-derived CNFs dominated the spectra. The carbon features confirmed the partial graphitization and the formation of CNFs. In contrast, the sharper, more symmetric Raman modes in MoS_2–HT reflected its highly ordered, defect-poor multilayer stacking, consistent with the prominent (002) reflection observed in the XRD results.[4,20] Corresponding nitrogen adsorption–desorption isotherms (Fig. S5a) showed that MoS_2|CNF–ES had a specific surface area of ≈ 180 $m^2\ g^{-1}$, nearly an order of magnitude higher than that of MoS_2–HT and MoS_2–HT/CNF (≈ 40 $m^2\ g^{-1}$), highlighting the effectiveness of the reduction–sulfidation sequence in generating hierarchical porosity and dispersing the active phases. The full results of the thermal analysis, including the BET surface area and TGA profiles, are provided in Figs. S5a,b and Table S1.

In addition, the morphology of the MoS_2|CNF-ES, MoS_2–HT, and MoS_2–HT/CNF catalysts was investigated using scanning electron microscopy (SEM; Figs. S6 and S7) and high-resolution transmission electron microscopy (HR-TEM; Figs. S8–S13). The SEM imaging revealed the continuous coverage of monolayer MoS_2 on the CNFs following sulfidation, whereas the hydrothermal samples retained a stacked morphology, and the hybrid material had an incomplete conformal coating. In the synthesis of the MoS_2|CNF–ES sample, the as-spun ATTM–PAN fibers formed uniform precursor filaments, which evolved into rigid CNFs decorated with MoS_2 when heated at 723 K under a H_2 atmosphere (Figs. S6a and S11a). Subsequent sulfidation in $H_2S/H_2/N_2$ at 973 K induced pore formation and exfoliation (Figs. S6b and S11b), producing a highly porous CNF network uniformly coated with a monolayer of MoS_2. In contrast, MoS_2–HT had a multilayer, densely stacked morphology (Fig. S7a), while the hybrid MoS_2–HT/CNF sample (Fig. S7b) contained heterogeneously distributed few-layered MoS_2 platelets that did not fully conform to the carbon fibers. These differences indicated that the electrospinning strategy enabled optimized control, resulting in highly dispersed MoS_2 within the catalyst.

HR-TEM, high-angle annular dark-field scanning transmission electron microscopy (HAADF-STEM), and energy-dispersive X-ray (EDX) mapping (Fig. 2; Figs. S8–S13) were used to investigate the nanoscale architecture of MoS_2|CNF–ES. HR-TEM and HAADF-STEM analysis confirmed the presence of atomically thin MoS_2 nanosheets uniformly distributed across the CNFs, with no evidence of restacking or aggregation. In line with this, EDX mapping showed homogeneous dispersion of Mo and S, with no

aggregated nanoparticles. In contrast, MoS_2–HT contained well-stacked multilayer lamellae with 0.62 nm (002) fringes, which was reflective of equilibrium-controlled growth and minimal defect density. MoS_2–HT/CNF exhibited few-layered MoS_2 clusters that assembled vertically and partially aggregated. The electron energy loss spectroscopy (EELS) spectra for MoS_2|CNF–ES (Fig. S12) revealed broader S $L_{2,3}$ and Mo $M_{4,5}$ edges, indicating the presence of defects in the sulfide structure, with under-coordinated Mo/S atoms. These features were significantly weaker in the hydrothermal and commercial catalysts.

X-ray photoelectron spectroscopy (XPS) analysis of Mo 3d spectra for all samples revealed dominant Mo^{4+} species (229.1 and 231.9 eV) characteristic of MoS_2,[21] with minor Mo^{6+} contributions (233.6 and 235.3 eV) from surface oxidation (MoO_3) and/or edge sites (Figs. 3a and S14).[4,22] The S 2p spectrum confirmed the presence of S^{2-} species, while MoS_2|CNF–ES exhibited an additional peak attributable to bridging disulfide (S_2^{2-}) ligands at the edges, consistent with an edge-rich structure that was also observed using in-situ diffuse-reflectance Fourier-transform infrared spectroscopy (DRIFTS) analysis (Fig. 3b).[23,24] The shift in the binding energy for Mo 3d and S 2p observed for MoS_2|CNF–ES and MoS_2–HT/CNF was indicative of strong sulfide–support interactions.

Quantitative nitric oxide (NO) chemisorption analysis confirmed that electrospinning enhanced both metal dispersion and defect accessibility (Table S1). MoS_2|CNF–ES had an adsorption rate of 132 $\mu mol_{NO}\ g_{cat}^{-1}$, roughly six times that of MoS_2–HT, while its O_2 uptake was also considerably higher, indicating a higher concentration of active sites associated with vacancies.[11,12] In-situ O_2 DRIFTS spectra (Fig. 3b) contained intense 960–900 cm^{-1} bands associated with terminal Mo = O groups at the edges for MoS_2|CNF–ES, whereas MoS_2–HT and MoS_2–HT/CNF contained additional 860–700 cm^{-1} features corresponding to in-plane Mo–O–Mo linkages on the basal plane.[12] The absence of these basal-plane modes in MoS_2|CNF–ES indicated that oxidation and vacancy formation were confined to the edges rather than distributed over the lattice. According to time-resolved DRIFTS analysis, these Mo = O bands remained stable with long-term O_2 exposure (Fig. 3c).

X-ray absorption near-edge structure (XANES; Fig. 3d) analysis of the MoS_2-based catalysts revealed similar edge positions for MoO_3 and Mo_2C, consistent with mixed + 4 and minor + 6 oxidation states and in accordance with the XPS results. Fourier transform–extended X-ray absorption fine structure (FT–EXAFS) (Fig. 3e) analysis revealed Mo–S (1.8–2.5 Å) and Mo–Mo (2.6–3.2 Å) coordination analogous to metallic Mo foil. In addition, quantitative EXAFS fitting (Table S2) suggested that MoS_2|CNF–ES had the lowest CN_{Mo-Mo}/CN_{Mo-S} ratio (0.70), indicating that it contained the highest fraction of coordinatively unsaturated Mo atoms. This reduced coordination likely originated from its monolayer structure and sulfide–support interactions, which stabilized the edge sites against sulfur replenishment.

Temperature-programmed in-situ XANES (Fig. 3f) analysis under a H_2 atmosphere revealed a progressive shift at the edges to a lower energy, confirming the H_2-induced reduction of Mo species and concomitant

sulfur removal. These edge defects served as dual-function centers, providing adsorption sites for H_2S and facilitating S–H bond activation, leading to the superior intrinsic activity and long-term stability observed during catalytic H_2S decomposition.[11,25]

Catalytic evaluation and structure–performance relationships

Evaluation of the catalysts under H_2S decomposition conditions (973 K, 1 bar) revealed that the synthesis pathway and interfacial structure had a strong influence on intrinsic activity (Fig. 4). Space–time adjustments were employed to account for variation in the bulk density, and equilibrium conversions were validated using Aspen Plus simulations (Figs. 4a, Figs. S3 and S4). MoS_2|CNF–ES achieved near-equilibrium H_2S conversion at a lower contact time, significantly outperforming both its hydrothermal (MoS_2–HT and MoS_2–HT/CNF) and commercial (MoS_2–Comm) counterparts (Figs. 4a,b). Intrinsic kinetic parameters were obtained from a kinetic model that accounted for equilibrium limits (Figs. 4c–e and Tables S3–S5), yielding a rate constant of 1.9×10^{-3} mol H_2S atm^{-1} g cat^{-1} s^{-1} for MoS_2|CNF–ES, which was 9-fold higher than MoS_2–Comm and 3-fold greater than MoS_2–HT and MoS_2–HT/CNF. The corresponding apparent activation energy (E_a ≈ 63 kJ mol^{-1}) was also markedly lower than that of the layered references, indicating facilitated H–S bond activation at the edge sites (Fig. 4d). Overall, MoS_2|CNF–ES had the highest activity, followed by MoS_2–HT, MoS_2–HT/CNF, and MoS_2–Comm, and it also compared favorably to previously reported catalysts (Table S6). The faster kinetics of MoS_2|CNF–ES likely reflected the highly dispersed nature of the active sites, with a high edge density, and their interactions with the support.

The intrinsic rate of H_2S decomposition also scaled linearly with NO chemisorption (Fig. 4f), establishing a quantitative link between catalytic performance and the density of coordinatively unsaturated Mo atoms. Because NO selectively binds to exposed Mo edge sites and sulfur vacancies, this correlation confirmed that the activity of MoS_2|CNF–ES was governed by accessible edge defects rather than the total Mo content. The similar proportionality between the rate constants and defect density derived from EXAFS coordination analysis and O_2 chemisorption (Table S1) confirmed that the concentration of sulfur vacancies was the dominant kinetic descriptor. The lower activation barrier of MoS_2|CNF–ES can be explained by its polarization at the sulfide–support interface, as evidenced by the XPS and XANES results (Figs. 4a,d–f). This interaction with the support weakens the Mo–S bonds at the edges, enhancing S–H bond dissociation and facilitating H_2 evolution. This interaction enables MoS_2 to maintain a reaction turnover without deactivation.

MoS_2|CNF–ES exhibited exceptional long-term stability, maintaining the steady-state conversion of H_2S feeds of varying concentrations (2–15 vol%) over 8 h and 50 h of continuous operation (Figs. 4g,h). The reaction rate fully recovered when reverting to the initial feed conditions, demonstrating the reversibility of sulfur accumulation. Post-reaction analysis confirmed the preservation of the structure and oxidation state of the proposed catalyst. XRD and XPS analysis (Figs. S14 and 4i) revealed unchanged 2H reflections and Mo^{4+}/Mo^{6+} ratios, while corresponding HR-TEM images contained intact monolayer

sheets without stacking or sintering. The carbon framework remained structurally robust, underscoring that the sulfide–support interaction suppressed both sulfur condensation and Mo migration, the principal deactivation pathways in conventional MoS_2 catalysts.

Density Functional Theory calculations: To evaluate how the graphene support influences H_2S activation, three basal-plane models were constructed: (i) a freestanding MoS_2 monolayer (ML–MoS_2), (ii) a freestanding bilayer (BL–MoS_2) representing a bulk-like configuration, and (iii) a graphene-supported MoS_2 monolayer (ML–MoS_2/graphene) simulating the experimentally observed CNF-supported catalytic domains (Fig. 5a). For each of these models, single sulfur vacancy (1-Vs) was generated by removing a top-layer S atom, while a second adjacent vacancy (2-Vs) was introduced to model multi-vacancy environments known previously as more catalytically active sites for S–H scission.[20,26] The corresponding optimized structures for the pristine, 1-Vs, and 2-Vs versions of the models are presented in Figs. S17–22.

The H_2S adsorption and dissociation energetics for all three systems are summarized in Figs. 5a,b. In the 1-Vs models, H_2S bound weakly to BL–MoS_2 (− 0.02 eV) and slightly stronger to ML–MoS_2 (− 0.20 eV) and ML–MoS_2/graphene (− 0.24 eV), indicating that both reduced dimensionality and the graphene interface enhance initial H_2S binding. The first S–H bond cleavage to form HS* + H* was mildly endothermic for all three 1-Vs systems (0.19–0.38 eV) together with the second cleavage leading to H* + H *+ S* formation (0.31–0.43 eV, Fig. 5b), though this was lowest for ML–MoS_2/graphene.

In contrast, all of the dissociation steps became exergonic at the 2-Vs sites. Across all models, the adsorption (− 0.32 to − 0.47 eV) and stepwise dissociation (− 0.34 to − 0.15 eV) of H_2S were thermodynamically favorable, demonstrating that multi-vacancy ensembles stabilize sulfur-containing intermediates and enable spontaneous S–H cleavage.

Graphene also promoted hydrogen-assisted vacancy formation (Fig. 5c). For 1-Vs, ΔE_{vac} decreased from + 0.01 eV (ML–MoS_2) and + 0.17 eV (BL–MoS_2) to − 0.03 eV for ML–MoS_2/graphene, confirming the stabilizing influence of the conductive support. Similarly, 2-Vs formation was most favorable for ML–MoS_2/graphene (− 0.62 eV), indicating that graphene promotes sulfur extraction under reductive conditions. Including finite-temperature corrections (973 K) from NIST thermochemical data reduced ΔG_{vac} by ~ 0.8 eV per sulfur atom, meaning that vacancy formation was thermodynamically feasible under the experimental activation conditions (Table S7).

Overall, these results demonstrate that graphene not only enhances H_2S binding but also lowers the energetic penalty for vacancy formation and sulfur dissociation. The ML–MoS_2/graphene system had the lowest energy barriers among the three models, providing a basis for accelerated H_2S decomposition at supported basal planes, consistent with our experimental findings.

DISCUSSION

Collectively, the operando, kinetic, and theoretical analyses produced a coherent mechanistic overview of H_2S decomposition on MoS_2-based catalysts. Within the electrospun MoS_2|CNF–ES catalyst, MoS_2 is grafted onto CNFs and interacts strongly with the support, resulting in active, stable S–H scission sites. As indicated by pulse chemisorption analysis, the electrospun catalyst has a far higher density of accessible Mo edge sites than either the hydrothermal or the bulk analogues. This enrichment likely arises from the electrospinning-induced grafting of MoS_2 precursors within polymer fibers, yielding uniformly dispersed monolayer MoS_2 domains following sulfidation. The resulting CNF architecture prevents sintering while introducing abundant defect sites. The sulfide-support interactions polarize the Mo–S bonds and weaken the S–H activation barrier, a phenomenon directly observed using in-situ spectroscopy. O_2-DRIFTS and XANES–EXAFS analyses suggest that sulfur vacancies form and heal dynamically under alternating H_2S/H_2 environments. The downshift of the Mo *K*-edge and the reduction in Mo–S and Mo–Mo coordination are indicative of the formation of undercoordinated MoS_2 centers. XPS corroborates this by identifying mixed Mo^{4+}/Mo^{6+} species stabilized by the support interface. These support interactions allow the edge vacancies to persist and remain catalytically active under conditions where unsupported MoS_2 rapidly deactivates.

DFT calculations provided atomistic support for this mechanism. The graphene-supported MoS_2 monolayer, which is an analogue of the CNF-grafted catalyst, has the lowest energetic cost for hydrogen-assisted sulfur removal (ΔE_{Svac} = − 0.03 eV for 1-V_S and − 0.62 eV for 2-V_S) and exergonic H_2S dissociation for all intermediates. The carbon substrate stabilizes these vacancies through support interactions, reducing the S-vacancy formation barrier and promoting continuous reactive turnover. According to finite-temperature corrections, vacancies form at 973 K, which was in line with the experimental observations of sustained activity and vacancy regeneration. The CNFs interact with the MoS_2 and stabilize the active sites. The faster kinetics of the MoS_2|CNF–ES catalyst arise from a high density of edge and vacancy sites and support interactions that stabilize these highly dispersed active sites.

CONCLUSIONS

The edge-enriched MoS_2|CNF catalyst developed in the present study delivered a 3-fold increase in H_2S decomposition activity and remarkable stability over 50 h of operation compared to bulk and hydrothermally synthesized MoS_2, while maintaining long-term stability under harsh conditions. This exceptional performance was due to the unique combination of (i) highly dispersed monolayer MoS_2 domains anchored on CNFs, (ii) strong sulfide–support interactions that suppress sintering and stabilize undercoordinated edge atoms, and (3) a dense population of sulfur vacancies. In situ spectroscopy and DFT calculations jointly confirmed that the stabilized edge vacancies serve as active sites for H_2S dissociation and hydrogen evolution. The proposed electrospinning–sulfidation route establishes a material-design paradigm for engineering metastable, edge-rich sulfides through confinement and stabilization. The grafting of sulfides onto CNFs and the resulting defect stabilization offer a transferable

blueprint for the synthesis of robust catalysts for other high-temperature, sulfur-tolerant hydrogen production processes.

METHODS

Catalyst synthesis

Three MoS_2-based model catalysts were prepared using hydrothermal and electrospinning methods reported in previous studies, with slight modifications and different pre-treatment protocols.[4,27,28]

Synthesis of MoS_2-HT

In the typical hydrothermal synthesis route, 0.8 mmol of ammonium heptamolybdate tetrahydrate (AMT; $(NH_4)_6Mo_7O_{24}$. $4H_2O$; Sigma-Aldrich; 99.98%) was dissolved in 30 mL of deionized (DI) water at room temperature and stirred for 30 min before the addition of citric acid (CA) or oxalic acid (OA); (0.05 g; Sigma-Aldrich; 99.5%) as a chemical agent under vigorous magnetic stirring for 20 min. The sulfide source (10 mmol of thiourea; CH_4N_2S; Sigma-Aldrich; 99.99%) was dissolved in another 30 mL of DI water at room temperature under vigorous magnetic stirring. The molybdenum solution was then added slowly to the sulfur solution, and the resulting mixture was transferred to a 100 mL Teflon-lined stainless-steel autoclave and heated at 473 K. After cooling to room temperature, the black product was filtered and washed several times with distilled water and absolute ethanol. The final product was dried at 333 K overnight. As a comparison, a commercial MoS_2 catalyst (98%, Alfa Aesar) was purchased from Thermo Scientific Chemicals and used as received for testing.

Synthesis of MoS_2|CNF–ES

MoS_2|CNF–ES was prepared using a modified electrospinning method.[28,29] PAN (1.0 g) and ATTM ($(NH_4)_2MoS_4$; 0.5 g) were dissolved in dimethylformamide to obtain PAN concentrations of 5, 10, or 15 wt/vol%. The precursor solutions were stirred for 24 h at 60°C until fully homogenized, and the resulting solutions were subsequently loaded into a syringe equipped with a 23-gauge stainless-steel needle. Electrospinning was conducted at a voltage of 15 kV with a flow rate of 1 mL h^{-1} and a tip-to-collector distance of 15 cm. The as-spun composite mats were collected on grounded aluminum foil and dried under a vacuum at 60°C. The obtained ATTM–PAN nanofibers were pre-treated at 723 K for 5 h in a H_2 (5 vol%)/N_2 (95 vol%) atmosphere, followed by further treatment at 973 K in 2 vol% H_2S/N_2 for 2 h and 50 vol% H_2/N_2 for 1 h with heating rates of 5°C min^{-1} for each treatment stage to obtain a porous MoS_2/CNF structure. As a comparison, after the first-stage heat treatment at 723 K for 5 h under H_2 (5 vol%)/N_2 (95 vol%), the resulting material was subjected to heat treatment at 973 K for 5 h under a N_2 atmosphere (Fig. S2).

Synthesis MoS_2–HT/CNF

CNFs were synthesized via electrospinning, followed by thermal treatment and the hydrothermal deposition of MoS_2. Initially, 1.0 g of PAN was dissolved in 7.0 g of DMF (Sigma-Aldrich, 99.8%) under continuous stirring for 24 h at room temperature. The resulting homogeneous solution was subjected to electrospinning to prepare the mats using the previously described process. The collected fibrous mats were pre-treated at 723 K for 5 h under a H_2 (5 vol%)/N_2 (95 vol%) atmosphere, followed by treatment at 973 K in 2 vol% H_2S/N_2 for 2 h and 50 vol% H_2/N_2 for 1 h with heating rates of 5 K min^{-1} for each treatment stage to obtain CNFs without MoS_2.

A hydrothermal method was employed for MoS_2 deposition, similar to the synthesis process for MoS_2-HT and a previously reported method.[30] Ammonium molybdate (15 wt% Mo) was dissolved in 30 mL of DI water and stirred for 30 min, followed by the addition of 0.05 g of OA under vigorous stirring for another 20 min. In parallel, 10 mmol of thiourea was dissolved in 30 mL of DI water. The molybdate solution was slowly added to the thiourea solution under stirring. The mixture was then transferred to a 100 mL Teflon-lined stainless-steel autoclave, and the required quantity of the CNF mat was added. The mixture was heated at 493 K for 18 h. After cooling, the product was filtered, washed with distilled water and ethanol, and dried overnight at 333 K.

Catalyst characterization

Crystallographic analysis was conducted via powder XRD in a Bruker D8 advanced diffractometer with a Bragg–Brentano geometry fitted with a Cu tube operating at 40 kV and 40 mA. Diffractograms were acquired over a 2θ range of 10–80° with a step size of 0.1° and a scan speed of 0.5 s per step. PDF-4+ (2019) was the database used for phase identification.

To investigate the textural properties of the samples, N_2 adsorption–desorption isotherms were obtained at 77 K using an ASAP 2040 instrument (Micromeritics). Before the measurements were taken, the samples were degassed for 10 h at 523 K. The specific surface area (S_{BET}) was determined from the isotherms using the Brunauer–Emmett–Teller (BET) equation.

The surface oxidation states of Mo and S were determined using XPS analysis in a K-ALPHA spectrometer (Thermo Scientific) with an Al-Kα (1486.6 eV) radiation source at room temperature under an ultra-high vacuum at 3 mA × 12 kV. The powder samples were pressed, mounted on the holder, and placed in the vacuum chamber. The C 1s peak at 284.5 eV was used to calibrate and correct the binding energy for the element, and charge compensation was achieved using a system flood gun, providing low-energy electrons. In addition, Raman spectra for the MoS_2 catalysts were obtained using a Renishaw Via Reflex confocal spectrometer with 532 nm laser excitation. The laser power was set to 5–10 mW, and the sample was irradiated for 10 s with six accumulations.

The catalyst morphology was investigated using HR-TEM with a Titan Themis-Z microscope (Thermo Fisher Scientific) at an accelerating voltage of 300 kV and a beam current of 0.5 nA. Dark-field (DF)

imaging employed an STEM and an HAADF detector. The STEM-HAADF data were collected at a convergence angle of 29.9 mrad and an HAADF inner angle of 30 mrad. Furthermore, an X-ray energy dispersive spectrometer (EDS) was utilized in conjunction with DF-STEM imaging to acquire STEM-EDS spectrum-imaging datasets and a post-column EELS instrument (GIF-Quantum 966; Gatan, Inc.).

NO chemisorption measurements were taken using a Micromeritics AutoChem II 2920 instrument.[11,12] In a typical fabrication route, 0.1 g of the catalyst sample was pretreated in situ under a flow of H_2 at 573 K for 3 h, followed by purging with He at the same temperature for 60 min. Subsequently, NO chemisorption was conducted at 313 K by pulsing 2% NO in He through the catalyst every 30 min. The NO signal was monitored via mass spectrometry and observed to increase until reaching a steady state, indicating saturation of the catalyst surface. The total NO uptake was then determined from the cumulative amount adsorbed.

O_2 pulse chemisorption experiments were performed with in-situ DRIFTS to quantify the active sites in the catalysts.[11,12] O_2 pulse titration was conducted using a Micromeritics Autochem II 2930. Typically, ~ 0.1 g of the catalyst was pretreated by H_2 at 573 K for 2 h and purged with He at 573 K for another 1 h. O_2 chemisorption was conducted at 313 K by pulsing 1 mL of 5% O_2/He over the catalyst every 15 min until peak saturation. Effluent O_2 was detected using a mass spectrometer until its level reached a constant value, representing O_2 saturation of the catalyst, after which the total uptake of O_2 was calculated.

In-situ DRIFTS measurements were taken on a Nicolet 6700 FTIR spectrometer with a liquid-nitrogen cooled MCT detector using a high-temperature reaction cell (Harrick) equipped with a temperature programmer and connected to a gas-dosing device with mass flow controllers (Bronkhorst). The catalyst was first reduced by pure H_2 at 573 K with a gas flow of 30 ml min^{-1} at 1 bar for 1 h and then cooled with He to 313 K for another 1 h. Spectra obtained at 313 K under a H_2 atmosphere were used as background spectra. Subsequently, the catalyst samples were treated with 5% O_2/He at a rate of 30 mL $min^{-1,}$ followed by spectra collection throughout in-situ DRIFTS.

Mo *K*-edge X-ray absorption spectra were recorded at room temperature using a Si (311) monochromator in the BL01B1 line of Spring-8 at the Japan Synchrotron Radiation Research Institute (JASRI) in Harima, Hyogo, Japan. The obtained spectra were analyzed and fitted using Athena and Artemis, which were equipped with ATOMS and FEFF6 in the software package Demeter 0.9.26.[31–33] After normalization at the edge height, the k^3-weighted χ spectra were extracted. Subsequently, these spectra in the k range of 3–14 $Å^{-1}$ were Fourier-transformed into the *R*-space. Curve-fitting analysis was conducted in an R range of 1.8–3.4 Å for Mo foil and 1.4–3.3 Å for all MoS_2 catalysts using the back-scattering amplitude and phase shift functions of Mo–Mo and Mo–S.

Catalyst testing

Catalytic H_2S splitting experiments were conducted using a PID testing unit with a fixed-bed quartz reactor (8 mm ID, length 340 mm) in down-flow mode (Fig. S23). The reactor was placed in a furnace, and the flow was controlled using a mass flow controller. In the reactor, ~ 0.03 g of sieved catalyst particles (100–150 μm) were loaded onto a 0.15 g SiC (particle grit 40) bed to ensure the catalyst bed rested in the isothermal zone of the reactor. The catalyst was pre-treated in situ first with a mixture of H_2S and H_2 (50:50) at 973 K for 1 h, followed by testing with a mixed feed containing 2 vol.% of H_2S at 1 bar in the temperature range of 773–973 K. A flow of 1 mL min^{-1} of He was added to the mixed feed as an internal standard. Reactor outputs were then analyzed using a Varian micro gas chromatograph with TCD detectors. The two-channel configuration and columns of this analytical system were used to quantify H_2, He, H_2S, and N_2. The conversion (X) is expressed as follows:

$$X_i\,(\%) = \frac{F_{i,0} - F_i}{F_{i,0}} \times\ 100$$

1

where $F_{i,0}$ is the molar flow rate at the inlet of the reactor of species *i* (e.g., H_2S), and F_i is the outlet molar flow rate of species *i*.

Simulations, kinetic model, rate constant, and turnover frequency calculations

The thermodynamic equilibrium conversion of H_2S under each tested condition was simulated using Aspen Plus with an R-Gibbs reactor and the WILSON base method. A kinetic model was used to describe the intrinsic reaction rate by integrating the rate expression over the catalyst weight. The rate constant (k) and activation energy (*E⍓*) were determined by minimizing the difference between the experimentally observed and theoretically predicted rates, ensuring an accurate fit to the data.

The turnover frequency (TOF) was calculated based on the initial reaction rate per active site. While the standard TOF expression assumes differential operation, we employed an alternative formulation suitable for near-equilibrium conditions, based on the initial rate at low conversion. Further details of model derivation, the fitting process, and TOF equations are provided in the Supporting Information.

Computational details

All spin-polarized density functional theory (DFT) calculations were performed using the Vienna Ab initio Simulation Package (VASP 5.4.4).[34] The projector-augmented wave (PAW) method was used to describe the interaction between core and valence electrons,[35] and generalized gradient approximation (GGA) in the Perdew–Burke–Ernzerhof (PBE) form was employed to account for exchange-correlation effects.[36]

Grimme's DFT-D3 method with Becke–Johnson damping was included in all calculations to capture dispersion interactions.[37]

The plane-wave kinetic energy cutoff was set to 500 eV, and the electronic energy convergence criterion was set to 10^{-5} eV. Structural relaxation was performed until the forces on all atoms were below 0.02 eV/Å. A vacuum layer of 15 Å was introduced along the *z*-direction to avoid spurious interactions between periodic images. The Brillouin zone was sampled using a Γ-centered Monkhorst–Pack k-point mesh of 3×3×1 for the (7×7) supercell models.[38]

Monolayer, bilayer, and graphene-supported monolayer MoS_2 systems were constructed to evaluate the effect of support and vacancy concentration. Sulfur vacancies (1-S and 2-S) were created by removing one or two surface S atoms, and the thermodynamic stability of various dissociated intermediates (H_2S*, HS* + H*, and H* + H* + S*) was evaluated. Adsorption energies were calculated relative to isolated gas-phase species and referenced to the pristine surface.

The sulfur vacancy formation energy (ΔEs_{vac}) was determined in the absence and presence of hydrogen co-adsorption to capture the thermodynamic impact of reductive conditions. The filling energy of vacancies with sulfur atoms (i.e., S-vacancy healing) was assessed to understand the post-dissociation stability of active sites.

The adsorption energy (E_{ads}) of a molecule or intermediate on the MoS_2 surface was calculated as follows:

$$E_{ads} = E_{slab+adsorbate} - E_{slab} - E_{adsorbate(g)}$$

2

where $E_{slab+adsorbate}$ is the total energy of the adsorbed system, E_{slab} is the energy of the clean surface, and $E_{adsorbate(g)}$ is the total energy of the isolated gas-phase molecule optimized in a large periodic box.

The sulfur-vacancy formation energy (ΔE_{Svac}) was computed as follows:

$$\Delta E_{Svac} - E_{vacant} - E_{pristine} + n\mu_S$$

3

where E_{vacant} and $E_{pristine}$ are the total energy of the defective and pristine MoS_2 slabs, respectively, *n* is the number of sulfur atoms removed, and μ_S is the sulfur chemical potential derived from gas-phase S_2:

$$\mu_S = \frac{1}{2} E_{S_2(g)}$$

4

Under reductive conditions, the hydrogen-assisted sulfur vacancy formation energy ($\Delta E_{Svac}^{H_2}$) was determined according to the following equation:

$$\Delta E_{Svac}^{H_2} = E_{vacant} - E_{pristine} + n\left(E_{H_2S(g)} - E_{H_2(g)}\right)$$

5

which represents the following process:

MoS_2 + n H_2 (g) → $MoS_{2-\square}$ + n H_2S (g) (6)

Eq. (5) therefore accounts for the removal of sulfur atoms from the surface through their conversion to H_2S gas in the presence of H_2.

To obtain temperature-corrected Gibbs free energies, the gas-phase DFT energies in Eq. (5) were replaced by temperature-dependent chemical potentials from the NIST-JANAF thermochemical tables:

$$\Delta G_{Svac}^{H_2(T,P)} = (E_{vacant} - E_{pristine}) + n\left[\mu_{H_2S}\left(T, p_{H_2S}\right) - \mu_{H_2}\left(T, p_{H_2}\right)\right]$$

7

where the temperature-dependent chemical potential of each gas is defined as shown in Eq. (8):

$$\mu_i(T, p_i) = \mu_i^{\circ}(T) + k_B T \ln\left(\frac{p_i}{p^{\circ}}\right)$$

8

and $\mu_i^{\circ}(T) = H_i^{\circ}(T) - TS_i^{\circ}(T)$ = H_i°(T) − TS_i°(T) was computed from NIST Shomate equations. For example, at 700°C (973 K) and 800°C (1073 K), $\mu_{H_2S}^{\circ}(T) - \mu_{H_2}^{\circ}(T)$ equals − 0.80 eV and − 0.89 eV, respectively.

DATA AVAILABILITY

The data supporting the findings of this article are available in the paper and the Supplementary Information. Additional data is available from the corresponding author on request. Source data are provided with this paper.

Declarations

AUTHOR INFORMATION

Authors and Affiliations

Multiscale Reaction Engineering, KAUST Catalysis Platform (KCP), King Abdullah University of Science and Technology (KAUST), Thuwal, 23955 – 6900, Saudi Arabia

Hend Mohamed, Vijay K. Velisoju, Muhammad Arief Shafarifky, Gontzal Lezcano, and Pedro Castaño

Water Desalination and Reuse Platform (WDRP), Division of Biological and Environmental Science and Engineering (BESE), King Abdullah University of Science and Technology (KAUST), Thuwal, 23955 – 6900, Saudi Arabia

M. Obaid and Noreddine Ghaffour

KAUST Catalysis Platform, King Abdullah University of Science and Technology (KAUST), Thuwal, 23955 – 6900, Saudi Arabia

Rafia Ahmed, Ildar Mukhambetov, Huabin Zhang, Polina Tolstova, and Luigi Cavallo

Department of Materials Engineering Science, Graduate School of Engineering Science, The University of Osaka, 1–3 Machikaneyama, Toyonaka, Osaka 560–8531, Japan

Yuma Hirayama and Takato Mitsudome

KAUST Core Labs, King Abdullah University of Science and Technology (KAUST), Thuwal, 23955 – 6900, Saudi Arabia

Mohamed Ben Hassine and Omar El Tall

Research and Development Center, Dhahran 31311, Saudi Aramco

Zainab Alaithan, Ali Almofleh, and Hassan Aljama

Chemical Engineering Program, Physical Science and Engineering (PSE) Division,

King Abdullah University of Science and Technology (KAUST), Thuwal, Saudi Arabia

Pedro Castaño

Contributions

H.M., V.K.V., H.A., and P.C. led the project and designed the experiments. H.M., M.O., and N.G. designed the materials and synthesis protocols using electrospinning. V.K.V. and H.M. performed and analyzed the basic characterization and contributed to the optimization of the thermal treatment of the catalysts.

V.K.V. performed and analyzed the catalytic testing, kinetic analysis, and advanced characterization. G.L. and V.K.V. contributed to kinetic model development. R.A., L.C., Z.A., P.T., and H.A. contributed to the theoretical calculations. V.K.V., H.M., and I.M. contributed to reactor operation, testing protocols, and analytical methodologies. M.B.H., O.E.T., and H.Z., contributed to material characterization, results interpretation, and manuscript reviewing. Y.H., M.A.S., and T.M. have conducted and analyzed the XAFS measurement. V.K.V., H.M., and P.C. wrote the manuscript with input from all authors. P.C. and H.A. were responsible for funding acquisition and project supervision.

Corresponding author

Correspondence to Pedro Castaño.

ETHICS DECLARATIONS

The authors declare no competing interests.

ACKNOWLEDGMENTS

All authors thank Saudi Aramco and King Abdullah University of Science and Technology (KAUST) for funding this work (RGC/3/5222–01 and BAS/1/1403) and for the resources in the supercomputing laboratory at KAUST. Y.H and T.M. received JSPS KAKENHI grant 23H01761 and JST PRESTO grant JPMJPR21Q9 for sources and funding of the synchrotron experiments (2025A1813).

References

1. Bligaard T et al (2016) Toward Benchmarking in Catalysis Science: Best Practices, Challenges, and Opportunities. ACS Catal 6:2590–2602
2. Vogt C, Weckhuysen BM (2022) The concept of active site in heterogeneous catalysis. Nat Rev Chem 6:89–111
3. Reverberi A, Pietro, Klemeš JJ, Varbanov PS, Fabiano B (2016) A review on hydrogen production from hydrogen sulphide by chemical and photochemical methods. J Clean Prod 136:72–80
4. Almofleh A et al (2025) Designing sulfide catalysts for H_2S dissociation to H_2 based on reaction descriptors and microkinetics. Appl Catal B Environ Energy 361:124605
5. Aljama H, Alaithan Z, Almofleh A (2023) Catalytic conversion of H_2S to H_2: Challenges and catalyst limitations. J Phys Chem C 127:9022–9029
6. Kraia T, Kaklidis N, Konsolakis M, Marnellos GE (2019) Hydrogen production by H_2S decomposition over ceria supported transition metal (Co, Ni, Fe and Cu) catalysts. Int J Hydrogen Energy 44:9753–9762
7. Deng D et al (2016) Catalysis with two-dimensional materials and their heterostructures. *Nat. Nanotechnol.* 11, 218–230 (2016)

8. Mao J, Wang Y, Zheng Z, Deng D (2018) The rise of two-dimensional MoS_2 for catalysis. Front Phys 13:1–19
9. Norskov JK, Christensen CH (2006) Toward efficient hydrogen production at surfaces. Sci (80-) 312:1322–1323
10. Voiry D et al (2013) Enhanced catalytic activity in strained chemically exfoliated WS_2 nanosheets for hydrogen evolution. *Nat. Mater.* 12, 850–855 (2013)
11. Hu J et al (2021) Sulfur vacancy-rich MoS_2 as a catalyst for the hydrogenation of CO_2 to methanol. Nat Catal 2021 43(4):242–250
12. Mao J et al (2023) Direct conversion of methane with O_2 at room temperature over edge-rich MoS_2. Nat Catal 2023 611(6):1052–1061
13. Hu J et al (2023) Edge-rich molybdenum disulfide tailors carbon-chain growth for selective hydrogenation of carbon monoxide to higher alcohols. *Nat. Commun.* 14, 1–11 (2023)
14. Zhou S et al (2023) Strained few-layer MoS_2 with atomic copper and selectively exposed in-plane sulfur vacancies for CO_2 hydrogenation to methanol. *Nat. Commun.* 14, 1–15 (2023)
15. Bojarska Z, Mazurkiewicz-Pawlicka M, Mierzwa B, Plocinski T, Makowski L (2022) Effect of the carbon support on MoS_2 hybrid nanostructures prepared by an impinging jet reactor for hydrogen evolution reaction catalysis. J Environ Chem Eng 10:108038
16. Obaid M et al (2020) Breakthroughs in the fabrication of electrospun-nanofiber-supported thin film composite/nanocomposite membranes for the forward osmosis process: A review. Crit Rev Environ Sci Technol 50:1727–1795
17. Pinilla JL, Purón H, Torres D, Suelves I, Millan M (2015) Ni-MoS_2 supported on carbon nanofibers as hydrogenation catalysts: Effect of support functionalisation. Carbon N Y 81:574–586
18. Cui J et al (2024) Carbon-anchoring synthesis of Pt1Ni1@Pt/C core-shell catalysts for stable oxygen reduction reaction. *Nat. Commun.* 15, 1–9 (2024)
19. Jagadale A, Zhou X, Blaisdell D, Yang S (2018) Carbon nanofibers (CNFs) supported cobalt- nickel sulfide ($CoNi_2S_4$) nanoparticles hybrid anode for high performance lithium ion capacitor. Sci Rep 8:1602
20. Zhou S et al (2024) Highly active single-layer 2H-MoS_2 for CO_2 hydrogenation to methanol. Appl Catal B Environ Energy 349:123870
21. Xu J et al (2023) Solution combustion synthesis of CoS_x, MoS_x, CoS_x-MoS_x and their catalytic activity in H_2 production from H_2S decomposition. Int J Hydrogen Energy 48:8807–8818
22. Hussain S et al (2016) Large-area, continuous and high electrical performances of bilayer to few layers MoS_2 fabricated by RF sputtering via post-deposition annealing method. Sci Rep 2016 61(6):1–13
23. Xu Q et al (2019) Unsaturated Sulfur Edge Engineering of Strongly Coupled MoS_2 Nanosheet–Carbon Macroporous Hybrid Catalyst for Enhanced Hydrogen Generation. Adv Energy Mater

9:1802553
24. Zheng Z et al (2020) Boosting hydrogen evolution on MoS_2 via co-confining selenium in surface and cobalt in inner layer. *Nat. Commun.* 11, 1–10 (2020)
25. Ozaki F et al (2023) Hydrogen-induced sulfur vacancies on the MoS_2 basal plane studied by ambient pressure XPS and DFT calculations. *ChemPhysChem* 24, e202300477
26. Kibsgaard J, Chen Z, Reinecke BN, Jaramillo TF (2012) Engineering the surface structure of MoS_2 to preferentially expose active edge sites for electrocatalysis. Nat Mater 11:963–969
27. Zheng X, Zhu Y, Sun Y, Jiao Q (2018) Hydrothermal synthesis of MoS_2 with different morphology and its performance in thermal battery. J Power Sources 395:318–327
28. Liu S et al (2012) Preparation of MoS_2 nanofibers by electrospinning. Mater Lett 73:223–225
29. Duan Y et al (2022) Embedding of ultra-dispersed MoS2 nanosheets in N,O heteroatom-modified carbon nanofibers for improved adsorption of Hg2+. Compos Commun 31:101106
30. Guan J et al (2022) Electrospinning derivative fabrication of sandwich-structured CNF/Co_3S_4/MoS_2 as self-supported electrodes to accelerate electron transport in HER. Int J Hydrogen Energy 47:14930–14941
31. Newville M (2001) IFEFFIT : interactive XAFS analysis and FEFF fitting. urn:issn:0909 – 0495 8:322–324
32. Ravel B (2001) ATOMS: crystallography for the X-ray absorption spectroscopist. urn:issn:0909 – 0495 8:314–316
33. Ravel B, Newville MATHENA (2005) ARTEMIS, HEPHAESTUS: data analysis for X-ray absorption spectroscopy using IFEFFIT. urn:issn:0909 – 0495 12:537–541
34. Kresse G, Furthmüller J (1996) Efficient iterative schemes for *ab initio* total-energy calculations using a plane-wave basis set. Phys Rev B 54:11169
35. Blöchl PE (1994) Projector augmented-wave method. Phys Rev B 50:17953
36. Perdew JP, Burke K, Ernzerhof M (1996) Generalized Gradient Approximation Made Simple. Phys Rev Lett 77:3865
37. Grimme S, Antony J, Ehrlich S, Krieg H (2010) A consistent and accurate ab initio parametrization of density functional dispersion correction (DFT-D) for the 94 elements H-Pu. J Chem Phys 132:154104
38. Monkhorst HJ, Pack JD (1976) Special points for Brillouin-zone integrations. Phys Rev B 13:5188

Figures

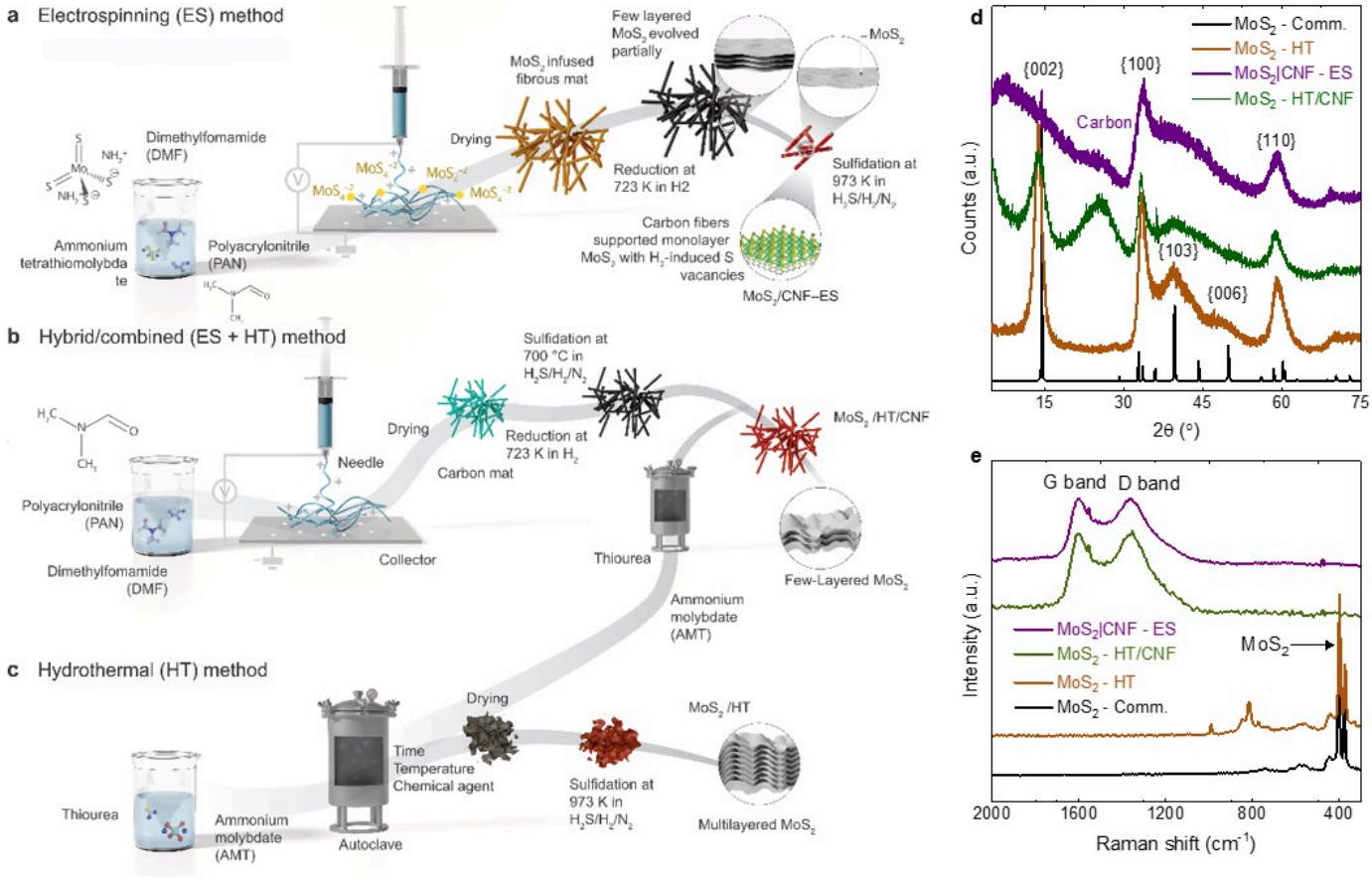


Figure 1

Schematic diagrams of catalyst selection and synthesis for bulk and supported MoS_2 catalysts using (a) electrospinning (ES), (b) hybrid, and (c) hydrothermal (HT) methods. (d) Powder X-ray diffraction (XRD) patterns and (e) Raman spectra for the catalysts after thermal treatment.

Image not available with this version

Figure 2

HR-TEM and HAADF-STEM-EDX analysis of and (a) MoS_2|CNF-ES, (b) MoS_2-HT/CNF, and (c) MoS_2–HT catalysts prepared using electrospinning, a hybrid route, and a hydrothermal method, respectively.

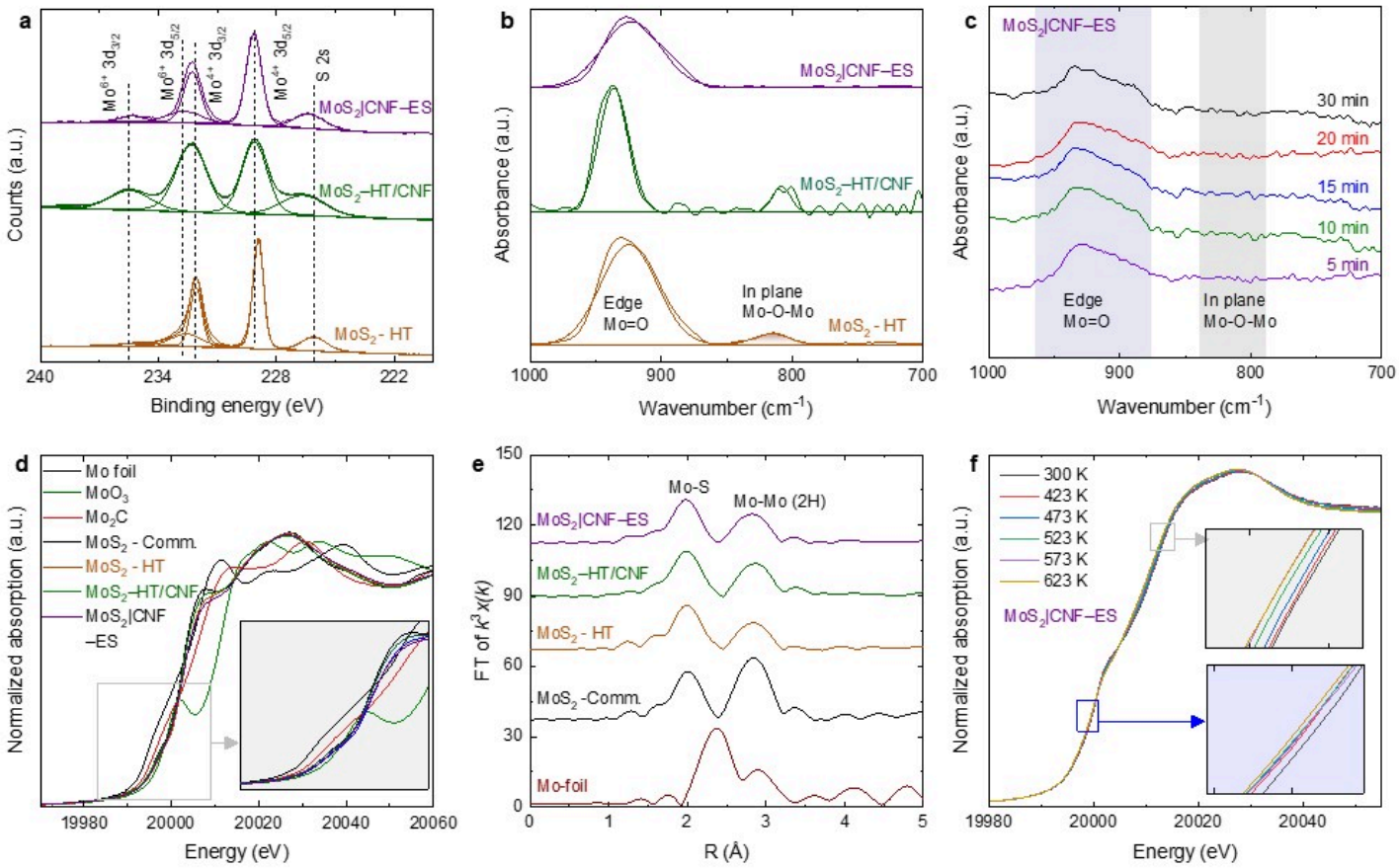


Figure 3

(a) Mo 3d spectra and (b) in-situ DRIFTS spectra for bulk and supported MoS_2 catalysts after oxygen adsorption at 313 K. (c) Time-resolved in-situ DRIFT spectra for MoS_2|CNF–ES after oxygen adsorption at 313 K. (d) XANES and (e) XAFS spectra for all catalysts. (f) In-situ XANES spectra for MoS_2|CNF–ES under a flow of H_2.

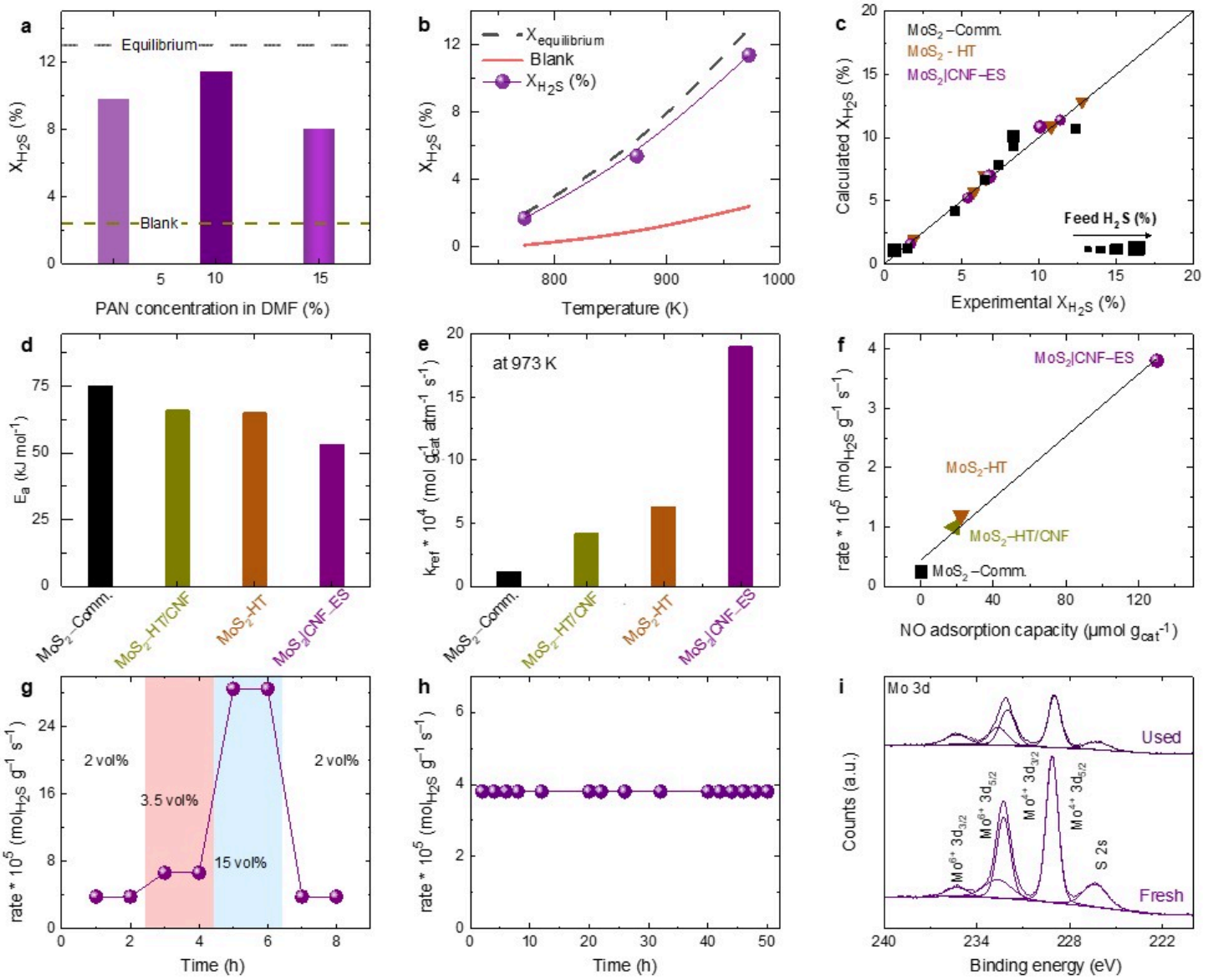


Figure 4

Activity of MoS_2|CNF–ES with different (a) PAN concentrations in DMF at 973 K and (b) reaction temperatures. Reaction conditions: Pre-treatment: 773–973 K in H_2S/H_2 for 2 h; H_2S feed: 2 vol% H_2S in N_2; reaction temperature: 973 K; and space time: 1.5 g_{cat} h mol_{H2S}^{-1}. (c) Parity plots, (d) activation energy, and (e) rate constants obtained from the kinetic model using the test data presented in Table S2. (f) Correlation between the H_2S decomposition rate and NO adsorption capacity obtained from NO chemisorption experiments. (g) H_2S conversion using the MoS_2|CNF–ES catalyst with a time on stream of 8 h and different concentrations of H_2S. (h) Time-on-stream analysis for 50 h for MoS_2|CNF–ES. Reaction conditions: Pre-treatment: 973 K in H_2S/H_2 for 2 h; H_2S feed: 2 vol% H_2S in N_2; reaction temperature: 973 K; and space time: 1.8 g_{cat} h mol_{H2S}^{-1}.(i) Mo 3d XPS spectra for MoS_2|CNF–ES before and after stability testing (50 h).

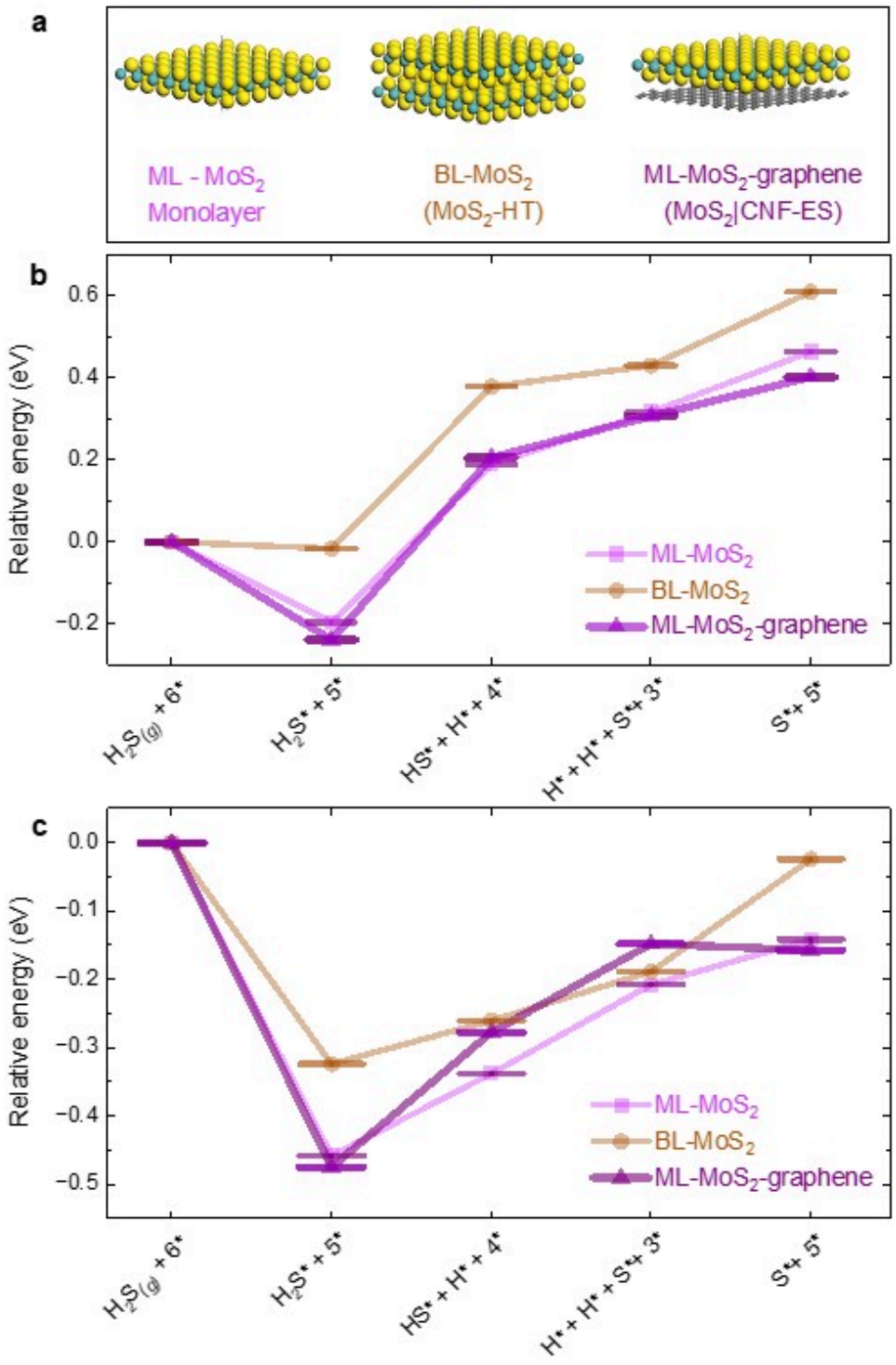


Figure 5

H_2S decomposition reaction profiles for monolayer, bilayer MoS_2, and graphene-supported monolayer MoS_2 model catalysts with both one and two sulfur vacancies: (a) catalyst models simulated using DFT calculations and reaction profiles for (b) one sulfur vacancy, and (c) two sulfur vacancies. The energies are reported at 0 K.

Supplementary Files

This is a list of supplementary files associated with this preprint. Click to download.

- 3SuppInfo.docx